RSC Advances

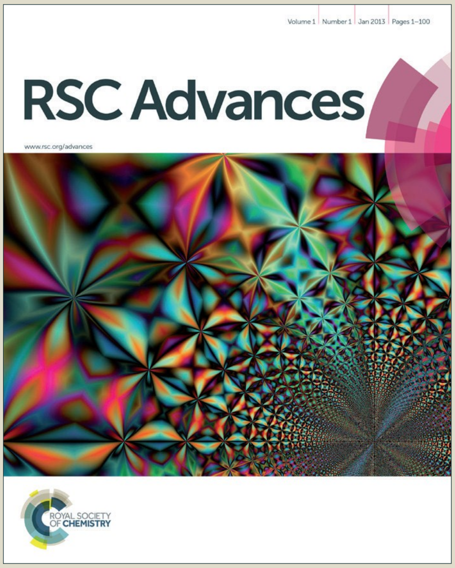

ROYAL SOCIETY
OF CHEMISTRY

www.rsc.org/advances

Journal Name

ARTICLE

Received 00th January 20xx,
Accepted 00th January 20xx

DOI: 10.1039/x0xx00000x

www.rsc.org/

Fabrication of micro/nanostructured α-Fe_2O_3 hollow spheres: Effect of electric field on morphological, magnetic and photocatalytic properties

Rich Kant, Neetesh Kumar and Viresh Dutta

In this paper, we reported the continuous fabrication of α-Fe_2O_3 hollow spheres with sponge like morphology using an electric field assisted (by applying DC voltage) continuous spray pyrolysis technique. The effect of applied voltage on the morphological, magnetic and photocatalytic properties are systematically studied. The samples prepared under electric field have shown enhanced magnetic and photocatalytic properties compared to the samples prepared without electric field (0kV). It is observed that the sample fabricated at an applied voltage of 2 kV has remarkably high coercivity (H_c) of ~4.5 kOe and manifested the maximum degradation efficiency of 98% and 95% under the visible light for methylene blue and rhodamine B dye, respectively owing to its sponge like morphology, enhanced surface area and pore volume. These α-Fe_2O_3 samples have potential applications in large memory devices, permanent magnets and efficient adsorbent materials for the removal of organic pollutants from water.

I Introduction

Fabrication of inorganic nanostructured materials with desired morphologies and properties has been attracting special attention in current years due to their wide range of scientific and technological applications. Among the diverse nanostructured morphologies, the hollow spheres are of great research importance because of their special optical, electrical, magnetic, thermal, electrochemical, photoelectrochemical, mechanical, catalytic properties and their wide range of applications such as in chemical storage, drug delivery, photonic crystals, waste removal, catalysis, gas sensors and low dielectric constant materials [1-16]. Recently the semiconductor and oxide catalysts in the form of hollow sphere are extensively applied in photocatalysis for wastewater purification, water disinfection, and perilous waste remediation. Numerous efforts have been made to fabricate hollow sphere photocatalysts, with variable sizes in the range from nano to microstructures to improve the photocatalytic properties. The micron-sized catalysts are constructed from very low dimensional reactive nanoparticles and have many advantages like high dispersion and easily recoverable, specifically high surface area and high activity of nanostructures. Several different kinds of nano and micro-structured materials have been synthesized and demonstrated with enhanced catalytic activity [17-23].

Hematite (α-Fe_2O_3) is highly stable and ecosystem friendly n-type semiconductor having band gap of 1.9 to 2.2 eV. It absorbs visible light up to 600 nm, and it is predicted that large light-harvesting efficiency and high photocatalytic activity could be achieved using hollow spheres as photocatalysts [17]. Moreover, as compared to other narrow band gap semiconductors (CdS, WO_3, $ZnIn_2S_4$ and Bi_2WO_6) [20–23], α-Fe_2O_3 exhibits higher perfect environmental compatibility, low cost and excellent stability against photo-corrosion in electrolyte solution [24]. Additionally, α-Fe_2O_3 powder can be easily separated from solution using magnetic field. Because of these interesting features, many types of micro and nanostructured α-Fe_2O_3 have been synthesized using self-assembly strategies [25–27], template methods [28–31]. However, these fabrication methods are generally time consuming and need substantial use of surfactant materials or laborious multi-step methods. Fabrication and designing of α-Fe_2O_3 in the form of hollow spheres with sponge like porous morphology would results into a great improvement in the photocatalytic activity. Due to porous nature of sponge like structures there will be easy dispersion of organic pollutants, which results into better interaction between the pollutant and iron oxide particles, certainly enhancing the photocatalytic activity [32].

Spray pyrolysis technique has been used several groups to synthesize the nano-micro structured oxide and semiconductor materials. Okuyama and Messing group have synthesized nano and microparticles/powders by spray-pyrolysis [33–35]. Suslik group has used ultrasonic pyrolysis to produce semiconductor and oxide nanocrystals [36–38].

Photovoltaic Laboratory, Centre for Energy Studies, Indian Institute of Technology Delhi, Room No-350, Block-V, HauzKhas, New Delhi- 110016, India.
E-mail: neetesh16@gmail.com; Fax: +91 11 2659 1261; Tel: +91 11 2659 6417

As per the best knowledge of the authors any research group does not report the fabrication of α-Fe_2O_3micro/nanospheres using electric field assisted continuous spray pyrolysis technique.

Although there are some reports on fabrication of α-Fe_2O_3 hollow spheres with various methods [39-45], here we present a surfactant and template free novel continuous spray pyrolysis (CoSP) technique for synthesizing α-Fe_2O_3 hollow micro/nanospheres with sponge like morphology. The electric field applied during the spray is shown to favourably affect the surface morphology. It is a one-step technique, which is very efficient in terms of time, cost and yield as compared to other template based, and hydrothermal techniques. The objective of the present work is to synthesize the α-Fe_2O_3 hollow micro/nano spheres through CoSP method and investigate the effect of electric field on structural, morphological magnetic and optical/photocatalytic properties. The photocatalytic ability of as α-Fe_2O_3 hollow micro/nano spheres using visible light source for the degradation of methylene blue (MB) has been investigated. The effect of electric field on the enhanced photocatalytic activity is also confirmed with rhodamine B dye (RhB).

II Experimental

Synthesis of hollow α-Fe2O3 micro/nanospheres

The chemicals were purchased from Fisher Scientific and used as received. The α-Fe_2O_3 hollow micro/nano spheres were synthesized by continuous spray-pyrolysis (CoSP) procedure using 0.15 M of Fe $(NO_3)_3.9H_2O$ dissolved in DI water at room temperature as the spray solution. The precursor solution was sprayed through the CoSP reactor consisting of three zones T1, T2 and T3 kept at different temperatures of 400°C, 900°C and 550°C, respectively [46]. Nitrogen was used as carrier gas at a pressure of 1kgf/cm^2 for atomization of the spray solution. An additional electrostatic pressure on spray droplets was created by applying a DC voltage (0 - 2kV) between an annular electrode and the nozzle (hence called the electric field assisted spray pyrolysis).The precursor solution was sprayed at a constant flow rate of 2.0 ml/min. The output products were collected in a DI water bubbler (trap) coupled at the outer end of the reactor. The samples prepared at different applied voltages of 0 kV, 1 kV and 2 kV are named as Fe_{0k}, Fe_{1k} and Fe_{2k}, respectively. The product were collected from trap by centrifugation and washed with deionized water. The product was dried in an oven at 60 °C overnight.

Characterization and measurements

The crystal structures of the products were investigated by X-ray diffraction studies using a Rigaku ULTIMA-IV diffractometer (with CuKα irradiation at a wavelength of 1.54056 Å) from 30° to 80°. The Raman spectra of all the samples were recorded by Horiba Lab RAM HR Evolution equipped with Ag ion 514nm laser at 20mW. FT-IR spectra were recorded by NICOLET iS50 FT-IR (ATR) spectrometer in the range of 400-4000 cm^{-1}. Field Emission Scanning Electron Microscope (FESEM) was used to analyze the morphology of the samples with Oxford-EDX system IE 250 X Max 80. Internal morphology, microstructure and elemental analysis (EDX) were investigated by the transmission electron microscopy (TEM) studies using FEI TecnaiTF20 electron microscope. N_2 adsorption-desorption isotherms were recorded on QuantachromeNovaWin Acquisition analyzer and reduction for NOVA instruments. Quantachrome instruments version 10.01 at 77K with nitrogen as analysis gas. Pore diameter and pore size distribution was calculated by using Barret-Joyner-Halenda (BJH) method. The absorption spectra were recorded with UV-Vis-NIR spectrophotometer (Perkin-Elmer Lamda-1050). Magnetization isotherms were measured in Quantum Design (PPMS Ever Cool-II) SQUID magnetometer in a magnetic field (H) up to 70 kOe. Magnetization (M) vs. temperature (T) measurements were performed in 10-300 K range following the zero field cooling (ZFC) and field cooling (FC) protocols in presence of constant field of 1kOe.The photocatalysis study was done by using ECIL India Double Beam UV-Vis Spectrophotometer (UV5704SS).

Assessment of Photocatalytic activity

The photocatalytic discoloration of methyl blue (MB) and rodhamine B (RhB) dyes was performed at ambient temperature in aqueous solution.In a typical procedure, in 20 ml of 3 × 10^{-5}mol/l MB solution, 10 mg of α-Fe_2O_3micro/nanospheres were dispersed, followed by addition of 0.1ml of hydrogen peroxide solution (H_2O_2, 30%). Samples were stirred in dark for 30 min to reach at equilibrium. Halogen lamp of 200 W with UV filter (15cm above the stirrer) was used as visible light source. 1.0 ml nanoparticles dispersed MB solution were collected out from the beaker after every 20 min at regular intervals and centrifuged at the same time for separation of dispersed nanoparticles. The absorbance of MB aqueous solution was determined by UV-Vis spectrometer, maximum absorption at 664 nm of MB dye. The photocatalytic degradation of RhB dye (5 × 10^{-5}mol/l RhB) was performed under the same experimental conditions as above.

The degradation efficiency R (%) was calculated using the following equation:

$$R= (C_0-C)/C_0 \times 100\% \qquad (1)$$

Where, C_0 is the dye initial concentration and C the dye concentration after photo-irradiation.

III Results and Discussion

Structure analysis of the products

Powder X-ray diffraction (XRD) study was conducted to identify the composition and crystalline phases in the final products fabricated at different voltages. Fig. 1 shows the XRD patterns of as- synthesized α-Fe_2O_3micro/nano hollow spheres. Sharp diffraction peaks in all the samples indicates that all samples are well crystalline in nature. The CoSP made α-Fe_2O_3samples have shown the rhombohedral structure with the reflection peaks from (104), (110), (113), (024), (116), (214) and (300) planes, with the lattice constant of a = b = 5.023 Å and c = 13.708 Å, which are in agreement with JCPDS 89-8104. It can be seen that in case of sample Fe1k peak intensity increases as compared to Fe0k with a further increase in case of Fe2k sample. This increase in diffraction peak intensity indicates the enhancement in crystalline nature of product with the applied voltage. Broadness of diffraction peaks i.e. Full width at half maximum (FWHM) increases with the applied voltage as a result of the crystallite size decrease. Average crystallite sizes are calculated from the Debye Scherrer formula D= 0.9λ/$\beta_{1/2}$ cosθ, where λ is the wavelength of X-rays and given in Table 1. Decrease in crystallite size with the applied voltage can be attributed to generation of smaller size droplets compared to zero applied voltage due to increased pressure on charged droplets also called Coulomb fission [47].

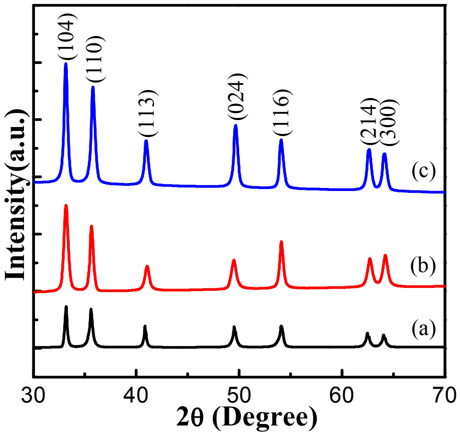

Fig. 1. XRD pattern of as synthesized α-Fe_2O_3 samples prepared at different applied voltages (a) Fe_{0k} (b) Fe_{1k} (c) Fe_{2k}.

Table 1: Structural parameters of α-Fe_2O_3 samples prepared at different applied voltages

Sample	**Fe_{0k}**	**Fe_{1k}**	**Fe_{2k}**
Crystallite Size (nm)	45.523	22	
Surface area (m^2/g)	8.3222.23	24	
Pore Diameter (nm)	1.8	1.9	2.4
Pore volume (cc/g)	0.078	0.135	0.153

Raman spectroscopy is used to verify the phase present in the samples. Peaks in the Raman spectra (Fig: 2) give confirmation of pure α-phase of Fe_2O_3 for all the samples, which is in consonance with XRD data. α-Fe_2O_3bands at 212 and 497 cm^{-1} corresponds to A_{1g} and the bands at 288, 402, and 605 cm^{-1} corresponds to $E_g$vibrational modes of α-Fe2O3 [48]. No signal from other iron oxide phases was observed in the Raman spectra confirming the pure α-Fe_2O_3 phase formation by CoSP technique at different applied voltages.

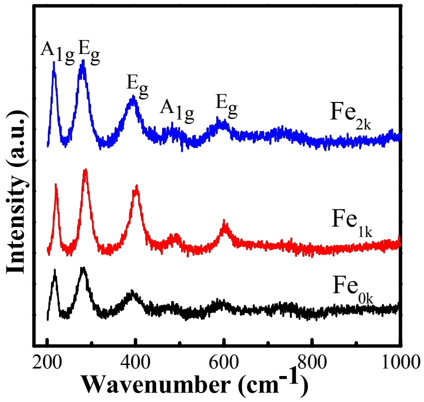

Fig. 2. Raman spectra of samples Fe_{0k}, Fe_{1k} and Fe_{2k}. Five strong peaks in the range of 200–1000 cm^{-1} can be assigned to the $2A_{1g}$ and $3E_g$ Raman active modes for the typical hematite phase.

The chemical compositions of α-Fe_2O_3samples prepared at different applied voltages were investigated by FT-IR spectroscopy shown in Fig. 3. Appearance of two major vibration bands in the range of 400-600 $cm^{-1}$of FT-IR spectrum confirms the formation of α-Fe_2O_3nano /microspheres. Vibration bands at ~434 cm^{-1} and ~525 cm-1 can be ascribed to stretching and bending vibration of Fe-O and Fe-O-Fe respectively [48]. The nonappearance of any extra absorption band in the FTIR spectrum again confirms the formation of pure α-Fe2O3 in all the samples prepared at different applied voltages.

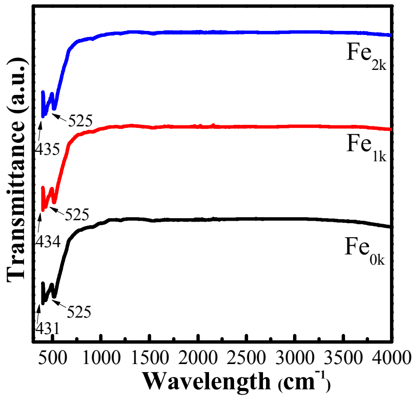

Fig. 3. FT-IR spectra of α-Fe_2O_3samples prepared at different applied voltages.

Morphology analysis

FE-SEM and TEM studies are performed to investigate the morphology and hollow structure of the α-Fe_2O_3 samples. Scanning electron microscopy (FE-SEM) images for Fe_{0k}, Fe_{1k} and Fe_{2k} are shown in Fig. 4. It is observed that sample grown in the absence of applied voltage (0.0 kV) displays solid spherical morphology with smooth surface and also having some pits on the surface on some of the particles. A voltage of 1.0 kV results in the formation of hollow α-Fe_2O_3 micro/nanospheres with broken shells and the number of hollow spheres increases for the applied voltage of 2.0 kV. Also surface of the spheres changes from smooth to porous sponge like (suggesting a higher surface area) in most of the particles for Fe_{1k} sample and almost all the particles in Fe_{2k} sample. It can be seen that in Fe_{0K} sample all the particles have particle size distribution in range of 0.1 to 2µm (due to large droplet size distribution).The uniform hollow spheres can be obtained by using spray nozzlesthat produces uniform droplets like ultrasonic nozzles.Since the applied voltage increases the charge density on the droplets resulting into formation of fine droplets, smaller size particles in the range of 100-500 nm are clearly visible for Fe_{1k} and Fe_{2k} samples.

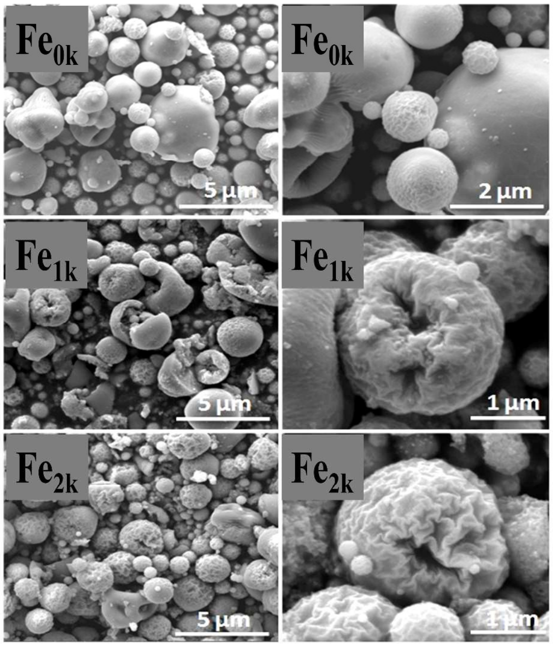

Fig. 4. Low and high magnification FE-SEM micrographs of Fe_{0k}, Fe_{1k} and Fe_{2k} samples prepared at different applied voltages.

The transmission electron microscopy (TEM) images, sectored area electron diffraction (SAED) patterns and energy dispersive X-ray (EDX) of α-Fe_2O_3samples prepared at different applied voltages are shown in Fig. 5. The images are dark because electron beam does not pass through the particles due to large size and thick shell. Increase in crystalline nature of samples with the electric field is further confirmed from the increase in ring pattern with bright spots in SAED patterns shown in Figure 5(b1-b3). Elemental composition is confirmed with EDX analysis shown in Figure 5(c1-c3), which indicates that as synthesized samples are composed of mainly Fe and O atoms with no other impurity. The Cu peaks visible in EDX images are due to copper grid.

Therefore, hollow α-Fe_2O_3 spheres with different microstructures and surface morphologies can be easily obtained by the way of applying an electric field on droplets during atomization. Outstanding reproducibility of this approach has been confirmed by doing repeated experiments and highly stable structures in terms of morphology and composition. These hollow structures with mesopores and sponge like surface structure should find useful application in catalysis and biotechnology. The sponge like morphology and internal particles structure of Fe_{2k} sample are shown in Fig. (6). The hollow structure should also be more efficient than other solid structures for these applications.

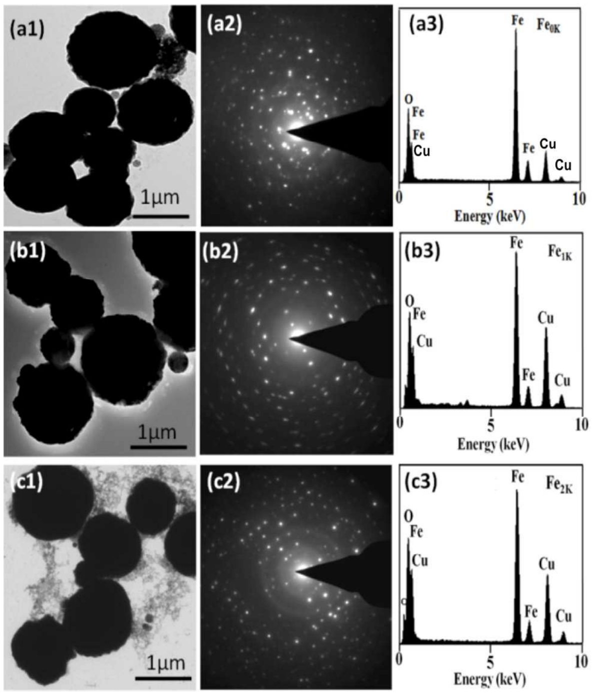

Fig. 5. Bright field TEM, SAED patterns and EDX images of Fe_{0k} (a1-a3), Fe_{1k} (b1-c1) and Fe_{2k} (c1-c3) samples.

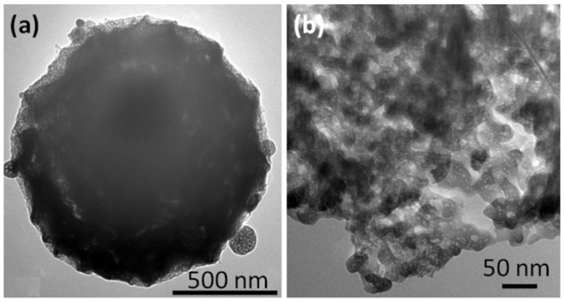

Fig. 6. High magnification TEM images of Fe_{2k} showing (a) sponge like morphology and (b) internal particles structure

Surface area and pore size characterization

Nitrogen adsorption-desorption isotherms were performed to determine the surface area and pore size of hollow α-Fe_2O_3spheres. Fig. 7 shows the typical nitrogen adsorption–desorption isotherms (77 K) for the samples prepared at different applied voltage (a) Fe_{0k}, (b) Fe_{1k} and (c) Fe_{2k}. All the isotherms were identified as the type IV, which is the feature of mesoporous materials [49]. The increase in nitrogen consumption for the samples Fe_{1k} and Fe_{2k} compared to Fe_{0k} at relative pressures (P/P_0) in the range 0.5-0.6 indicates the enhancement in porous structure in the samples, which also supports the FESEM data. Surface area, average pore radius and pore volume values are given in Table 1. It can be seen that there is a continuous increase in values of surface area, pore diameter and pore volume with the applied voltage. This can be attributed to formation of unique hollow and sponge like porous morphology of α-Fe_2O_3 micro/nano spheres having lower nanoparticle size due to the applied voltage as compared to α-Fe_2O_3 micro/nano spheres prepared in the absence of the applied voltage. The higher surface area and pore volume offer more reaction sites and higher adsorption, resulting in better photocatalytic activity.

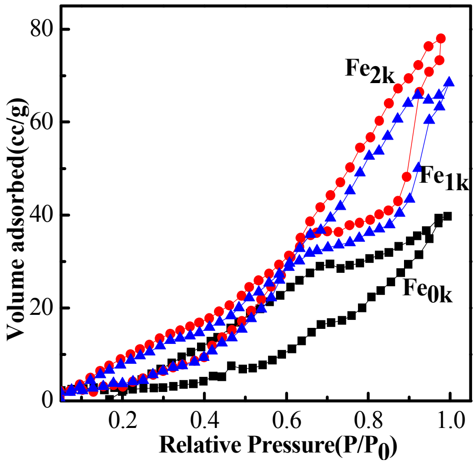

Fig. 7. N_2 adsorption–desorption isotherms for Fe_{0k}, Fe_{1k} and Fe_{2k} samples.

Optical properties

The optical absorption of the α-Fe2O3 micro/nanospheres were studied at room temperature using Ultraviolet-Visible spectroscopy (Fig. 8). Pronounced absorption at the wavelengths shorter than 700 nm can be attributed to the intrinsic absorption band gap of α-Fe2O3 due to the electron transitions from O2p valence band to Fe3d conduction band, indicating that α-Fe_2O_3 micro/nanospheres can work as photocatalyst under the visible light. Fig.8 displays the UV-Vis absorption spectra of the samples prepared at different applied voltage. The $(\alpha h\nu)^2$ versus photon energy (hν) is also plotted in the inset of Figure 8. It can be seen that absorption shoulder at 560 nm for Fe_{0k} appears to be blue shifted to 550 nm for Fe_{1k} sample and it further shifted towards 545 nm for Fe_{2k} sample.This shift can be attributed to decrease in the nanoparticle size because of the decrease in droplet sizes with the applied voltage. From the extrapolation of linear portion of curves of $(\alpha h\nu)^2$versus photon energy (hν) the value of band gap is determined to be 1.95eV, 1.97eV and 2.05eV for Fe_{0k}, Fe_{1k} and Fe_{2k}, respectively. Increase in band gap corresponding to absorption maxima with applied voltage can be ascribed to reduced particle/ crystallite size as obtained from TEM and XRD studies.

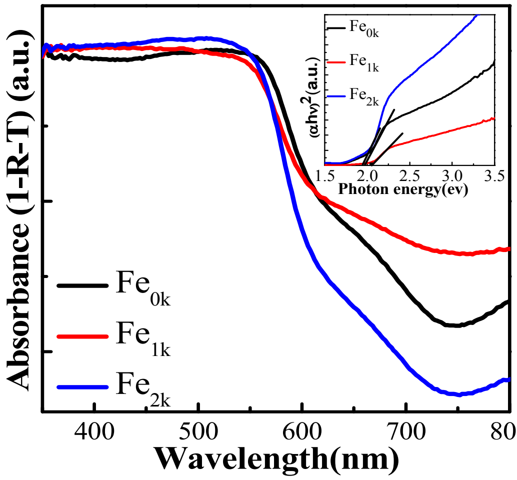

Fig. 8. Absorption spectra of samples Fe_{0k}, Fe_{1k} and Fe_{2k}. Inset shows the Tauc plots.

Magnetic properties

Fig. 9 shows the magnetic hysteresis (M vs. H) behavior of the Fe_{0k}, Fe_{1k}, and Fe_{2k} samples recorded at 300 K, with the magnetic field sweeping from -70 kOe to 70 kOe. It can be seen that M-H curves at 300 K for all the samples do not reach to the saturation even at a maximum applied field. All the M-H curves are showing hysteric behavior with non-zero remanence magnetization (Mr) (see inert Fig. 9). The values of squareness ($S= M_r/M_{70kOe}$) are 0.08, 0.09 and 0.09 with coercivity values of 2.2, 3.5, and 4.5 kOe for Fe_{0k}, Fe_{1k}, and Fe_{2k} samples, respectively. This kind of magnetic behavior is indicative of ferromagnetic particles present in the all the samples [46]. It may be pointed out that H_C increases with the applied voltage during growth. The remarkable high H_C observed in Fe_{1k} and Fe_{2k} samples (Fig. 9b & 9c) can be attributed to the observed sponge like porous morphology in FESEM micrographs. This kind of porous structure results in the large number of smaller particles present in α-Fe_2O_3particles, the presence of this sub-structure is reported to be the cause of high value of HC in samples Fe_{1k} and Fe_{2k} samples [50].

Fig. 10 shows the iso-field temperature (T) dependence of the magnetization (M) for all the samples, recorded in ZFC and FC protocols in the presence of 1 kOe magnetic field. The presence of broad peak in Fe_{0k} sample with blocking temperature (TB) = 100 K and a transition generally known as

Morin transition [51] is observed at Morin Temperature (TM) = 230 K (determined from derivative FC curve, insert Fig. 10(a)). The TB is observed in samples having small superparamagnetic particles and the observed non-saturating M-H behavior supports this observation [52]. TM is a phase transition of α-Fe_2O_3particles, above which it behaves as weak ferromagnetic [53]. The simultaneous presence of TB and TM in Fe_{0k} sample indicates the presence of superparamagnetic and ferromagnetic particles. The shift of TB towards lower temperature is indicative of the decrease in the size of superparamagnetic particles with the applied voltage.

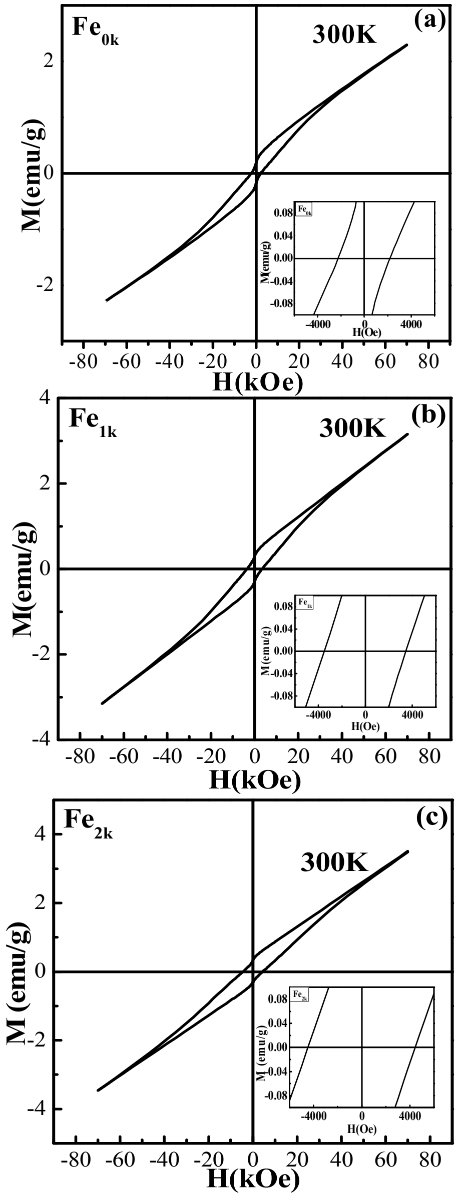

Fig. 9. M–H loops recorded at 300 K for (a) Fe_{0k}, (b) Fe_{1k} and (c) Fe_{2k}. The insets show extended view near the low field regime highlighting the presence of hysteresis.

In addition to this, the effect of applied voltage during growth can also be seen as the dominance of Morin transition over superparamagneticbehavior as height of peak corresponds to superparamagneticbehavior starts to decrease compared to Morin transition. This indicates that weakly ferromagnetic particles dominance is increasing over the superparamagnetic particles. So, we can say that the applied voltage is responsible for the reduction of particles contributing to superparamagneticbehavior (which is generally observed in systems having particle size smaller than 20 nm) [51], but at the same time it promotes the porous nature of the particles and hence the sub-structure. This observation is in consonance with the observation high HC values observed in Fe_{1k} and Fe_{2k} samples.

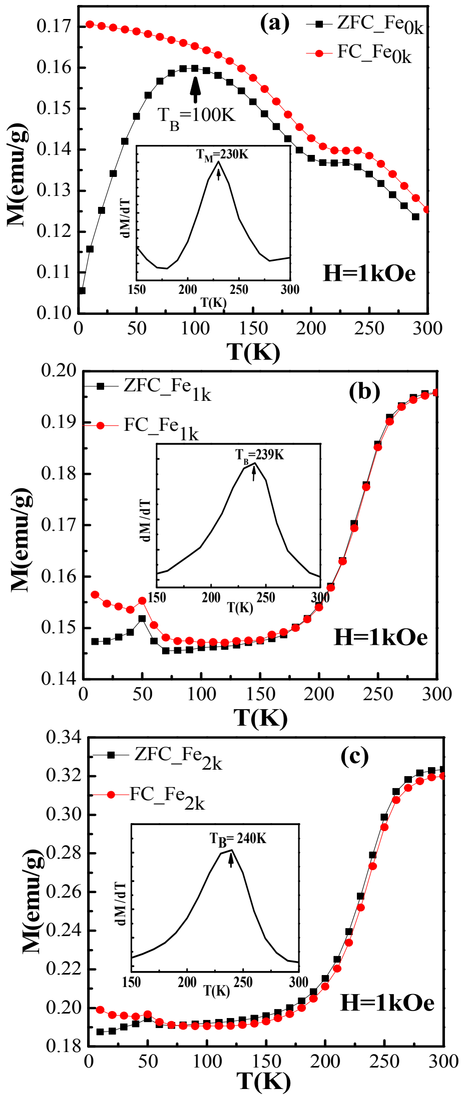

Fig. 10. Temperature dependence of ZFC and FC magnetization for (a) Fe_{0k}, (b) Fe_{1k} and (c) Fe_{2k}. Insets are corresponding differential ZFC curves.

Visible light photocatalytic activity

Assessment of photocatalytic activity of the α-Fe_2O_3samples prepared through CoSP technique was done by photodegradation of the MB dye with visible light in the presence of H_2O_2.

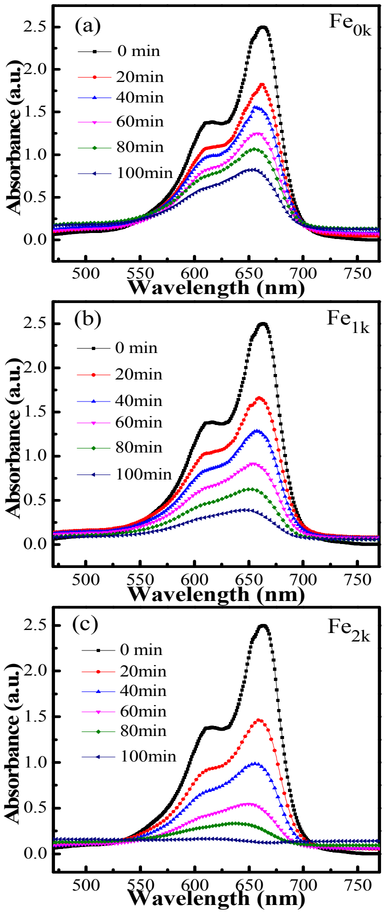

Fig. 11. UV-Vis absorption spectra of MB dye under visible light at different intervals of time for Fe_{0k}, Fe_{1k} and Fe_{2k} samples.

Fig.11 shows the UV-Vis spectra of MB aqueous solution displaying photo-degradation at different time intervals in the presence of α-Fe_2O_3 samples prepared at different applied voltages. The MB dye displays two major absorption bands at 664 nm and 610 nm. Change in intensity of the absorption maxima of the MB dye with the time is considered as a measure for the determination photocatalytic performance of the α-Fe_2O_3 samples. Absorbance change was negligible for all the samples when MB dye solution was kept in dark indicating the requirement of light for dye degradation. Blank experiment was performed without photocatalyst in the presence of H_2O_2 only, very small change in absorbance was observed as compared to the samples with α-Fe_2O_3 micro/nanospheres. It is clearly inferred from Fig.11 that Fe_{2k} sample is the most active photocatalyst in the degradation process as after 100 min complete oxidation of the MB dye has occurred and no absorption band could be seen in the presence of hollow α-Fe_2O_3micro/nanospheres. This can also be attributed to the lowest crystallite size, highest surface area and porosity as compared to the other samples α-Fe_2O_3solid spheres prepared at 0kV applied voltage (Fe_{0k}) expectedly exhibit weaker performance in terms of discoloration of MB dye as compared to hollow spheres prepared at 1kV (Fe_{1k}) and 2_{kV} (Fe_{2k}) applied voltage. It is known that distinct hollow and porous structures allow efficient transportation of charge carriers to the surface of nanospheres and also multiple reflections from the shells of the porous hollow spheres results into efficient light absorption [53].

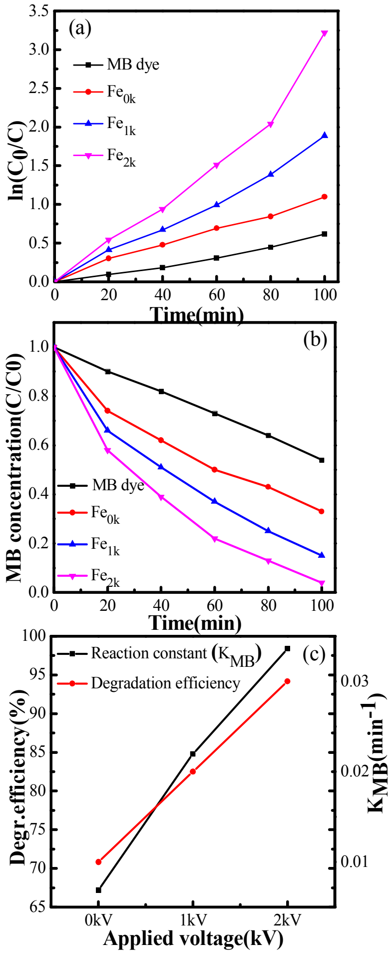

Fig. 12. (a) C/C_0 curves of the aqueous MB dye solution versus irradiation time (b) ln (C/C_0) of dye degradation versus irradiation time (c) degradation efficiency and pseudo first order rate constants (k_{MB}) of α-Fe_2O_3samples prepared at different applied voltage.

To understand the kinetics of photodegradation normalized concentration of MB (C/C_0) versus irradiation time is plotted in Fig. 12(a), where C_0 is the initial concentration of dye and C is the concentration of dye at different intervals of time. It is evident from the trend of exponential fall that the samples prepared with the voltage applied are more effective in photodegradation of dye. It is well known that first order kinetics is followed for photodegradation of organic pollutants, which is expressed as ln $(C/C_0) = k_{MB}t$ [54] where $k_{MB}$is apparent rate constant. The linear relationship between ln (C/C_0) and t shows that photodegradation reaction follows the Pseudo first order reaction (Fig. 11(b)). It can be seen that the value of rate constant $k_{MB}$is minimum i.e. 0.01 min^{-1} in case Fe0k sample which increases to 0.02 min^{-1} for Fe_{1k} and 0.03 min^{-1} for Fe_{2k} samples (see Fig.12(c)). The reason for increase in rate constant again is the improvement of microstructure (porous and sponge like morphology) with the applied voltage.

The photocatalysis study revealed that maximum degradation (98.4%) of the dye is achieved in case of Fe_{2k} sample in 100 min (Fig. 12(c)). Also 84.8% of dye degradation is achieved for Fe_{1k}sample, which is comparatively better as compared to the sample, prepared at zero applied voltage (Fe_{0k}).

Mechanism of degradation can be expressed as:

$MB + hv \longrightarrow MB^*$ (2)

$MB^* + \alpha\text{-}Fe_2O_3 \longrightarrow MB^{\bullet+} + \alpha\text{-}Fe_2O_3\ (e^-_{CB})$ (3)

$\alpha\text{-}Fe_2O_3\ (e^-_{CB}) + O_2 \longrightarrow O_2^{\bullet-} + \alpha\text{-}Fe_2O_3$ (4)

$\alpha\text{-}Fe_2O_3 + hv \longrightarrow \alpha\text{-}Fe_2O_3\ (e^-_{CB}, h^+_{VB})$ (5)

$H_2O_2 + e^-_{CB} \longrightarrow OH^- + OH^\bullet$ (6)

$h^+V_B + OH^- \longrightarrow OH^{*-}$ (7)

$MB^*/\ MB^{\bullet+} + (OH^\bullet, OH^{*-}, O_2^{\bullet-}) \longrightarrow$ degradation products (8)

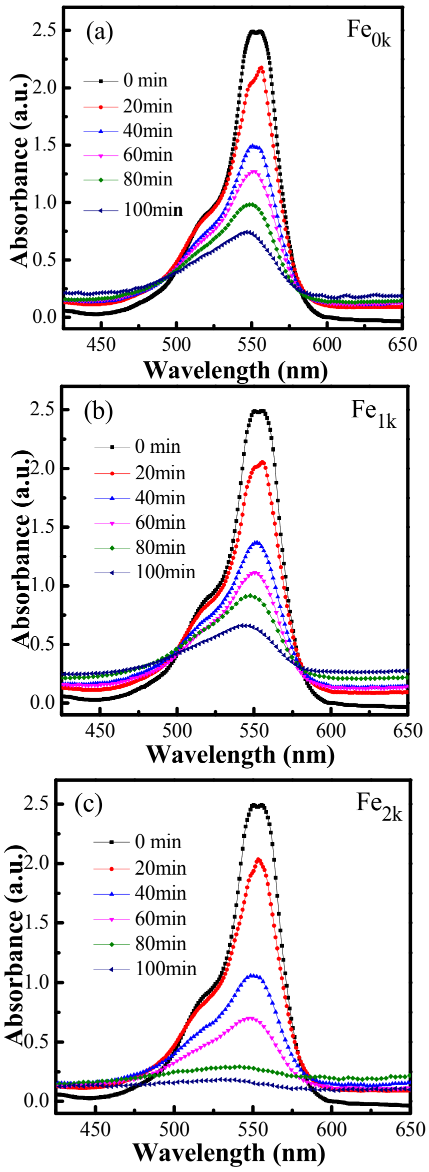

Fig. 13. UV-Vis absorption spectra of RhB dye under visible light at different intervals of time for Fe_{0k}, Fe_{1k} and Fe_{2k} samples.

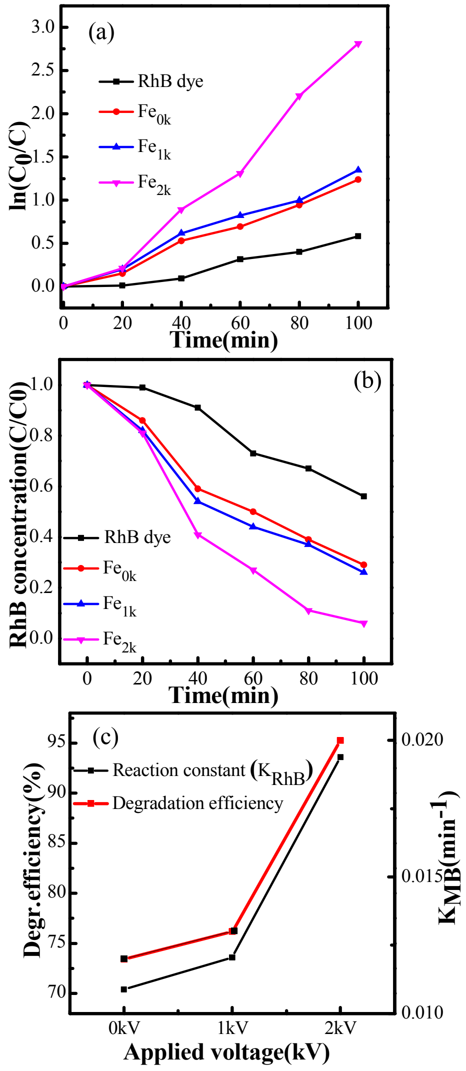

Fig. 14. (a) C/C_0 curves of the aqueous RhB dye solution versus irradiation time (b) ln (C/C_0) of dye degradation versus irradiation time (c) pseudo first order rate constants (k_{RhB}) and degradation efficiency of $\alpha\text{-}Fe_2O_3$ samples prepared at different applied voltage.

Table 2: Degradation efficiency and rate constant for MB and RhB dyes

Sample Name	Degradation Efficiency (%)	Rate Const. (min^{-1})	Degradation Efficiency (%)	Rate Const. (min^{-1})
	MB Dye		RhB Dye	
Fe_{0k}	67.0 ± 1.3	0.01	73 ± 1.8	0.011
Fe_{1k}	84.8 ± 1.2	0.02	77 ± 1.7	0.012
Fe_{2k}	98.4± 1.5	0.03	95 ± 2.1	0.019

Mechanism of heterogeneous photocatalysis is generally initiated either through light absorption from photocatalyst or organic dye molecule. In our case it can be observed that photodegradation of MB dye in the presence of α-Fe_2O_3 micro/nanospheres could be due to absorption of light from dye molecule followed by photocatalyst. Initially upon absorption of visible light, MB dye is excited to singlet or triplet states (eqn.2) followed by charge transfer from the dye to conduction band of photocatalyst (α-Fe_2O_3) (eqn.3) where photogenerated electrons (e^-) of α-Fe_2O_3 are easily transferred to oxygen on the catalyst surface resulting into formation of oxide radical ($O_2^{\bullet -}$) (eqn.4). Now the light absorption occurs through α-Fe_2O_3 generating electron and hole pair (eqn.5). In the next step photogenerated electrons (e^-) of α-Fe_2O_3 trapped in the presence of H_2O_2 and results into formation of. OH radicals (eqn.6), which triggers the photocatalytic reaction. Photogenerated holes (h^+) reacts with OH^- to form hydroxyl radical ($OH^{-\cdot}$) on the surface of catalyst (eqn.7). Finally dye reacts interact effectively with $^{\cdot}OH$, $O_2^{\bullet -}$ and $OH^{\bullet -}$ Species and undergo mineralization into nontoxic organic compounds (eqn.8) [17, 55].

The photocatalytic activities of Fe_{0k}, Fe_{1k} and Fe_{2k} samples were also examined with RhB dye under visible light illumination. The intensity of the characteristic absorption peak in the absorption spectrum at 555 nm decreased continuously with the irradiation time shown in Fig.13. The quantitative analysis of RhB photodegradation is analyzed by plotting RhB (C/C_0) versus irradiation time, ln (C/C_0) versus t, degradation efficiency and apparent rate constant (K_{RhB}) in Fig. 14(a), 14(b) and 14(c), respectively. Degradation efficiency and rate constant for MB and RhB dyes are presented in the Table-2. It can be concluded from above plots that Fe_{2k} sample again performs the best among all samples in terms of photocatalytic degradation of RhB dye and results in complete oxidation of RhB dye in 100 mins. All the results confirm the high photodegradation efficiency of α-Fe_2O_3nano/microspheres towards both MB and RhB dyes. Hence the samples prepared by the novel electric field assisted continuous spray pyrolysis (CoSP) technique can prove efficient photocatalysts for discoloration of textile effluents and water purification.

IV Conclusions

Sponge like nano/microstructured α-Fe_2O_3 hollow spheres with sponge morphology has been synthesized via CoSP technique under applied voltage and their application in photocatalytic decomposition of MB and RhB dyes under visible light irradiation has been studied. The magnetic and photocatalytic activity of Fe_{2k} sample was found to be superior to that of other nanostructures of α-Fe_2O_3 reported earlier. The photocatalytic study show that the dyes maximum discoloration ability of the CoSP prepared α-Fe_2O_3 under electric field turned out to be more than 95% within 100 min for both MB and RhB dye. The surprising good results are due to the smaller crystallite size with increased surface area, higher crystallinity, hollow structure and sponge like surface morphology. Hollow spheres with sponge like porous structures give the benefit of having more sites for easy dispersion and better interaction between the effluent and photocatalyst and thus are effective towards water decontamination. The low-cost, high yield, easy and continuous fabrication methodology of α-Fe_2O_3 and other materials like FeS magnetic hollow spheres of with such novel structures should be of great interest for the applications in the different areas such as nanotechnology, biomedical, adsorbents and catalysis.

Acknowledgements

Government of India for award of MNRE fellowship is gratefully acknowledged. We thankfully acknowledge Prof.SujeetChaudhary for PPMS EVERCOOL-II facility at IIT Delhi and Dr. Dinesh Kumar for magnetic data analysis.

References

1. F. Caruso, Adv. Mater. 2001, 13, 11.
2. J. Hu, M. Chen, X, Fang and L. Wu, Chem. Soc. Rev., 2011, 40, 5472.
3. Y. Zhao and L. Jiang, Adv. Mater. 2009, 21, 3621.
4. X. Jiang, T. L. Ward, Y. S. Cheng, J. Liu and C. J. Brinker, Chem. Commun., 2010, 46, 3019.
5. W. Wei, G. H. Ma, G. Hu, D. Yu, T. Mcleish, Z. G. Su, Z. Y. Shen, J. Am. Chem. Soc., 2008, 130, 15808.
6. J. Shin, R. M. Anisur, M. K. Ko, G. H. Im, J. H. Lee, I. S. Lee, Angew. Chem. Int. Ed. 2009, 48, 321.
7. B. Wang, J. S. Chen, H. B. Wu, Z. Wang, X. W. Lou, J. Am. Chem. Soc., 2011, 133, 17146.
8. X. W. Lou, D. Deng, J. Y. Lee, L. A. Archer, Chem. Mater., 2008, 20, 6562.
9. L. Ye, C. Wu, W. Guo, Y. Xie, Chem. Commun., 2006, 4738.
10. Y. Z. Zhu, Y. L. Cao, Z. H. Li, J. Ding, J. S. Liu, Y. B. Chi, J. Colloid Interface Sci., 2007, 306, 133.
11. J. F. Galisteo-López, M. Ibisate, R. Sapienza, L. S. Froufe-Pérez, A. Blanco, C. López, Adv. Mater. 2011, 23, 30.
12. L. Wang, S. A. Asher, Chem. Mater., 2009, 21, 4608.
13. J. Cao, Y. Zhu, L. Shi, L. Zhu, K. Bao, S. Liu, Y. Qian, Eur. J. Inorg. Chem., 2010 1172.
14. Y. Li, T. Kunitake, S. Fujikawa, J. Phys. Chem. B, 2006, 110, 13000.
15. X. L. Li, T. J. Lou, X. M Sun, Y. D. Li, Inorg. Chem., 2004, 43, 5442.

16. J. Zhang, S. Wang, Y. Wang, M. Xu, H. Xia, S Zhang, W. Huang, X. Guo, S. Wu, Sensors and Actuators B, 2009, 139, 411.
17. J. Yu, X. Yu, B. Huang, X. Zhang, Y. Dai, Cryst. Growth Des. , 2009, 9, 1474.
18. E. Hosono, S. Fujihara, H. Lmai, I. Honma, I. Masaki, H. Zhou, ACS Nano., 2007,1, 273.
19. J. Yu, X. Yu, Environ. Sci. Technol., 2008, 42, 4902.
20. H. Zhang, Y. Zhu, J. Phys. Chem. C, 2010, 114, 5822.
21. L. Li, M. Krissanasaeranee, S. W. Pattinson, M. Stefik, U. Wiesner, U. Steiner, D. Eder, Chem. Commun., 2010, 46, 7620.
22. Z. Lei, W. You, M. Liu, G. Zhou, T. Takata, M. Hara, K. Domen C. Li, Chem. Commun. 2003, 17, 2142.
23. J. Wu, F. Duan, Y. Zheng Y. Xie, J. Phys. Chem. C., 2007, 111, 12866.
24. R. Krol, Y. Liang, J. Schoonman, J. Mater. Chem., 2008, 18, 2311.
25. B. Sun, J. Horvat, H. S. Kim, W. S. Kim, J. Ahn, G. Wang, J. Phys. Chem. C., 2010, 114, 18753.
26. L.P. Zhu, H. M. Xiao, X. M. Liu, S. Y. Fu, J. Mater. Chem., 2006, 16, 179.
27. R. Zhang, H. Dai, Y. Du, L. Zhang, J. Deng, Y. Xia, Z. Zhao, X. Meng, Y. Liu, Inorg. Chem., 2011, 50, 2534.
28. X. W. Lou, L. A. Archer, Z. Yang, Adv. Mater., 2008, 20, 3987.
29. L. Jia, W. Cai, H. Wang, J. Mater. Chem., 2009, 19, 7301.
30. F. Li, J. He, W.L. Zhou, J. B. Wiley, J. Am. Chem. Soc., 2003, 125, 16166.
31. F. Jiao, A. Harrison, J. C. Jumas, A. V. Chadwick, W. Kockelmann, P. G. Bruce, J. Am. Chem. Soc., 2006, 128, 5468.
32. L. P. Zhu, L. L. Wang, N. C. Bing, C. Huang, L. J. Wang, G. H. Liao, ACS Appl. Mater. Interfaces, 2013, 5, 12478.
33. K. Okuyama, I. W. Lenggoro, Chem. Eng. Sci., 2003, 58, 537.
34. G. L. Messing, S. C. Zhang, G. V. Jayanthi, J. Am. Chem. Soc., 1993, 76, 2707.
35. B. Xia, I. W. Lenggoro, K. Okuyama, Adv. Mater., 2001, 13, 1579.
36. S. S. Dunkle, R. J. Helmich, K. S. Suslick, J. Phys. Chem. C, 2009, 113, 11980.
37. Y. T. Didenko, K. S. Suslick, J. Am. Chem. Soc., 2005, 127, 12196.
38. W. H. Suh, K. S. Suslick, J. Am. Chem. Soc., 2005, 271, 2007.
39. S. Y. Lian, E. B. Wang, L. Gao, D. Wu, Y.L. Song, L. Xu, Mater. Res. Bull., 2006, 41, 1192 .
40. L. L. Li, Y. Chu, Y. Liu, L. H. Dong, J. Phys. Chem. C, 2007, 111, 2123.
41. J. H. Bang, K. S. Suslick, J. Am. Chem. Soc. 129 (2007) 2242-2243.
42. B. D. Mao, Z. H. Kang, E. B. Wang, C. G. Tian, Z. M. Zhang, C. L. Wang, Y. L. Song, M. Y. Li, J. Solid State Chem. 2007, 180, 489.
43. S. Li, H. Zhang, J. Wu, X. Ma, D. Yang, Crystal Growth & Design, 2006, 6, 351.
44. L.P. Zhu, N.C. Bing, L.L. Wang, H.Y. Jin, G.H. Liao, L.J. Wang, Dalton Trans., 2012, 41, 2959.
45. S. Zeng, K. Tang, T. Li, Z. Liang, D. Wang, Y. Wang, Y. Qi, W. Zhou, J. Phys. Chem. C, 2008, 112, 4836**.**
46. N. Kumar, V. K. Komarala, V. Dutta, Chem. Eng. J., 2014, 236, 66.
47. N. Kumar, V. K. Komarala, V. Dutta, PSSRRL, 2012, 6, 406.
48. R. Kant, D. Kumar, V. Dutta, RSC Adv., 2015, 5, 52945.
49. K. S. W Sing, D. H. Everett, R. A. W. Haul, L. Moscou, R. A. Pierotti, J. Rouquerol, T. Siemieniewska, Pure & Appl. Chem., 1985, 57, 603.
50. C. Rath, K. K. Sahu, S. D. Kulkarni, S. Anand, S. K. Date, R. P. Das, N. C. Mishra, Appl. Phys. Lett., 1999, 75, 4171.
51. P. G. Bercoff, H. R. Bertorello, Appl. Phys. A, 2010, 100, 1019.
52. D. Kumar, S. Chaudhary, D. K. Pandya, J. Magn. Magn. Mater., 2014, 370, 127.
53. J. Zhuang, Q. Tian, H. Zhou, Q. Liu, P. Liu, H. Zhong, J. Mater. Chem., 2012 22, 7036.
54. G. Liu, Q. Deng, H. Wang, D. H. L. Ng, M. Kong, W. Caia, G. Wang, J. Mater. Chem., 2012, 22, 9704.
55. Y. Huang, D. Ding, M. Zhu, W. Meng, Y. Huang, F. Geng, J. Li, J. Lin, C. Tang, Z. Lei, Z. Zhang, C. Zhi, Sci. Technol. Adv. Mater., 2015, 16, 014801.

Graphical Abstract

Continuous fabrication of α-Fe_2O_3 hollow spheres with sponge like morphology using an electric field assisted (by applying DC voltage) continuous spray pyrolysis (CoSP) technique. Sample fabricated at an applied voltage of 2 kV has remarkably high coercivity (H_C) of ~ 4.5 kOe and maximum degradation efficiency of 98% and 95% under the visible light for methylene blue (MB) and rhodamine B (RhB) dyes, respectively.